Article

Facet-Controlled Growth of Hydroxyapatite for Effectively Removing Pb from Aqueous Solutions

Hee Jung Kim,[||] Jin Hyuk Choi,[||] SangMyeong Lee, Gill Sang Han,* and Hyun Suk Jung*
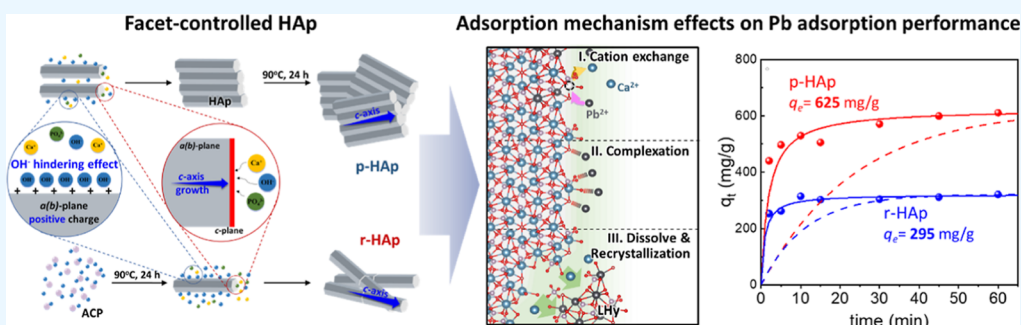
Read Online

ACCESS | Metrics & More | Article Recommendations | SI Supporting Information

ABSTRACT: To address the growing concerns regarding severe water pollution, effective and environmentally friendly adsorbents must be identified. In this study, we prepared hydroxyapatite (HAp, $Ca_{10}(PO_4)_6(OH)_2$) as an eco-friendly absorbent via simple precipitation and obtained rod- (r-HAp) and plate-shaped HAp (p-HAp). The approach to obtaining p-HAp involved a low pH titration rate, promoting growth along the c-axis due to the adsorption of OH^- on the (110) facet. Conversely, r-HAp was obtained by maintaining a high concentration of OH^- during the initial stage through rapid pH titration, leading to a stronger restrictive effect on the growth of positively charged $a(b)$-planes. p-HAp demonstrated superior adsorption capacity, removing Pb through dissolution and recrystallization, achieving an impressive 625 mg/g within a 60 min reaction time compared to r-HAp. Our findings afford insights into the Pb removal mechanisms of HAp with different morphologies and can aid in the development of water purification strategies against heavy metal contamination.

1. INTRODUCTION

Water pollution is a severe environmental concern that can accelerate the water shortage and threaten the environmental ecosystems involving water. Heavy metals are notable water pollutants as they are nondegradable and can bioaccumulate. Lead, listed by the World Health Organization as one of the ten chemicals of public health concern, is a toxic heavy metal that can directly affect the brain, kidneys, nerves, and bones.[1−5] Several approaches for removing pollutants have been developed, for example, adsorption,[6,7] chemical precipitation,[8,9] reverse osmosis,[10,11] ion exchange,[12−14] and membrane-based purification.[15−18] Among these methods, adsorption is a promising strategy for water purification owing to its low cost, simplicity, universality, recycling, and reusability. Many absorbents, such as metal oxides,[7,19−21] biochar,[22−24] carbons,[25,26] zeolite,[27,28] and calcium phosphate,[29−31] have been developed to remediate heavy-metal-contaminated water.

Hydroxyapatite (HAp, $Ca_{10}(PO_4)_6(OH)_2$), an eco-friendly biomineral, is one of the most promising absorbents, as it has the highest absorption capacity for heavy metals. The adsorption performance of HAp is strongly influenced by structural properties such as crystallinity, defects, surface texture, specific surface area, and morphology. The lower

crystallinity observed leads to increased active surface area[32] and weaker chemical bonds,[33] contributing to enhanced adsorption properties. Additionally, the low crystallinity introduces a large number of defects, making the material highly degradable. Consequently, Ca ions are easily released from HAp, facilitating ion exchange with other metal ions.[34] Xu et al.[35] employed manganese-doped HAp (MnHAp) to enhance heavy metal adsorption performance. The low-concentration doping of Mn caused lattice distortion and a substantial number of defects, as smaller Mn ions substituted for Ca ions, resulting in an enhanced adsorption capacity. The heavy metal removal mechanism and performance strongly depend on the morphology of HAp,[36−39] as different morphologies are associated with different specific surface areas, mechanical properties, and surface characteristics. Many researchers have attempted to develop HAp with different

morphologies, such as rod, plate, dandelion, and spherical particles, by controlling the specific facet growth using anionic or cationic surfactants. Hao et al.[40] studied the Pb removal performance of rod- (r-HAp), flake-flower-, and dandelion-shaped HAp. The use of ammonium tartrate and trisodium citrate surfactants resulted in the formation of flake-flower and dandelion morphologies, respectively. In contrast, r-HAp was obtained when no surfactants were used. The dandelion-shaped HAp exhibited the highest maximum adsorption capacity of 819.7 mg/g, owing to the presence of multiple adsorption sites. However, the surfactants used in synthesizing HAp affect its physical and chemical properties such as the surface area, acid sites, and Ca/P ratio,[41] which considerably influence the Pb removal ability. Additionally, the high sorption capacity of mesoporous nano-HAp for Pb (1438.85 mg/g) was reported.[42] Removal and reuse of Pb were realized using Fe-decorated HAp high sorption capacity with fast kinetics.[30] Recently, whitlockite (WH, $Ca_{18}Mg_2(HPO_4)_2(PO_4)_{12}$), with a similar phase as that of HAp, was introduced as an adsorbent for removing Pb.[29] WH exhibits a higher Pb adsorption capacity (2339 mg/g) than HAp despite a smaller Brunauer−Emmett−Teller (BET) surface area, potentially because the dissolution and recrystallization mechanisms are in play. Nonetheless, despite the numerous studies on controlling the shape of HAp, there has been limited research conducted to understand the influence of HAp morphology on the Pb adsorption performance.

In this study, we aimed to realize the facet-controlled growth of HAp nanoparticles (NPs) using a simple precipitation method without any surfactants. The HAp morphology was noted to depend on the initial pH conditions. At high pH values, the initial phase transformed from amorphous nuclei to r-HAp, whereas under low initial pH conditions, plate-shaped HAp (p-HAp) was obtained, forming hexagonal apatite. The Pb adsorption performance associated with the different morphologies was investigated in terms of their kinetic models and Pb removal mechanisms. The results indicated that p-HAp removes Pb with dissolution and recrystallization as the main mechanisms. In contrast, the Pb removal mechanism of r-HAp changes from initial complexation with Pb to dissolution and recrystallization over time. Consequently, p-HAp exhibits an adsorption capacity of 625 mg/g, which is two times that of r-HAp (294.99 mg/g), which demonstrates the higher effectiveness of p-HAp in Pb removal.

2. EXPERIMENTAL SECTION

2.1. Materials. Calcium nitrate tetrahydrate ($Ca(NO_3)_2 \cdot 4H_2O$, 99%), sodium dihydrogen phosphate dihydrate ($NaH_2PO_4 \cdot 2 H_2O$, 99%), gelatin (from bovine skin, Type B), sodium hydroxide (NaOH, 98%, pellets), and lead nitrate ($Pb(NO_3)_2$, 99%) were purchased from Sigma-Aldrich and used without purification.

2.2. HAp Synthesis. p-HAp and r-HAp were synthesized via precipitation methods. For p-HAp, $NaH_2PO_4 \cdot 2 H_2O$ (0.15 mol/m³) and gelatin (0.5 g) were dissolved in 250 mL of deionized water heated to 40 °C and mixed with a solution of $Ca(NO_3)_2 \cdot 4H_2O$ (0.25 mol/m³) dissolved in 250 mL of deionized water. Subsequently, 20 cm³ of a sodium hydroxide (NaOH) solution (1 mol/m³) was added in a dropwise manner using a syringe pump, and the solution was maintained at 40 °C for 24 h. To obtain r-HAp, NaOH (1 mol/m³) was poured into a solution prepared in the same manner as

aforementioned until the pH became 7.5. The solution was heated to 90 °C and maintained at this temperature for 24 h.

2.3. Characterization. The morphologies and elemental distribution of samples were investigated by field emission scanning emission microscopy (FE-SEM) and energy dispersive spectroscopy (EDS)-based elemental mapping (JSM-7600F, JEOL Ltd.). The crystal phases of all the samples were analyzed by X-ray diffraction (XRD) (Rigaku, SmartLab SE) patterns obtained at a scanning rate of 4°/min and step of 0.02°, and the crystallite size was calculated using the Scherrer equation.[43,44]

$$L = \frac{K\lambda}{\beta \cdot \sin \theta}$$

where L is the crystallite size, K is a constant related to crystallite shape (normally taken as 0.9), λ is the wavelength of X-ray, β is the full-width half-maximum (FWHM), and θ is the diffraction angle.

The morphology and crystal structure of the synthesized samples were determined by transmission electron microscopy (TEM) and selected area electron diffraction (SAED), and the *d*-spacing was calculated through high-resolution transmission electron microscopy (HR-TEM) (JEM-ARM200F, JEOL Ltd.). The zeta potential in a neutral aqueous solution was determined using an electrophoresis analyzer (ELSZ2000-ZS, Otsuka) by the Doppler method. The Hückel equation was used[45] and each measurement was conducted three times for accuracy.

2.4. Pb Removal Experiments. Pb solution was prepared by dissolving $Pb(NO_3)_2$ in deionized water at concentrations of 400 mg/m³ and 2100 mg/m³. The synthesized p-HAp and r-HAp were added to Pb solutions with concentrations of 2100 mg/L in dosages of 1 g/m³. The samples were dispersed by sonication for 2 min. Each sample was allowed to react with Pb ions for durations ranging from 10 min to 24 h. After the reaction, the solutions were filtered, and the concentrations of Pb and Ca were measured through inductively coupled plasma-atomic emission spectrometry (OPTIMA 8300, PerkinElmer).

For the analysis of adsorption kinetics, we employed the pseudo-first-order (PFO) and pseudo-second-order (PSO) models.[46−48] The adsorption capacities were calculated using the following equation

$$q_t = (C_0 - C_t)V/m$$

where C_0 is the initial concentration, C_t is the remaining concentration, V is the volume of solution, and m is the adsorbent mass.

The PFO kinetics are described by the following equation

$$\log(q_e - q_t) = \log q_e - (k_1 t)/2.303$$

where q_e is the equilibrium absorption capacity, q_t is the absorption capacity at each contact time t, and k_1 is the PFO constant. This equation can also be defined as

$$q_t = q_e(1 - \exp(-k_1 t))$$

The PSO kinetics are given by the following equation

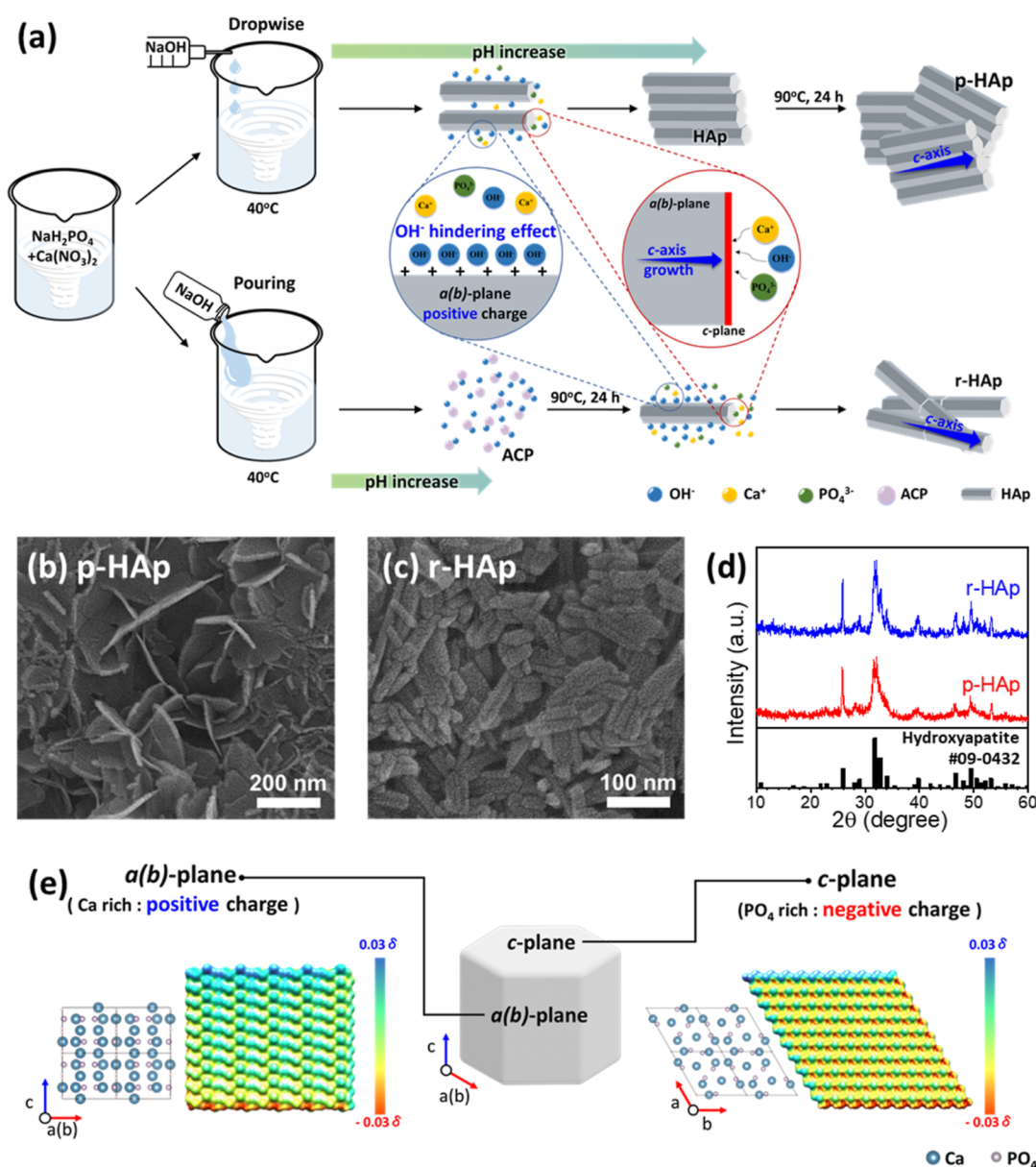$$q_t = q_e \frac{k_2 q_e t}{1 + k_2 q_e t}$$

Figure 1. (a) Schematic of HAp synthesis by adjustment of the pH. FE-SEM images of synthesized (b) p-HAp and (c) r-HAp. (d) XRD patterns of as-synthesized samples. (e) Crystal structures and molecular electrostatic potential surface mappings corresponding to the $a(b)$-plane and c-plane of HAp.

where q_e is the equilibrium absorption capacity, q_t is the absorption capacity at each contact time t, and k_2 is the PSO constant. This equation can also be defined as

$$q_t = q_e \frac{k_2 q_e t}{1 + k_2 q_e t}$$

2.5. Simulations. Simulations were conducted to examine the crystal structures of HAp. The optimized data of all crystal structures were derived from the Materials Project [hydroxyapatite (mp-41472)].[49] Avogadro 2 was used to obtain the simulation data for molecular electrostatic potential mapping.[50] Other simulation data were obtained by Quantum Espresso, an open-source density functional theory calculation software package in Materials Square. The molecular electrostatic potential mapping was simulated using a $5 \times 5 \times 1$ superlattice of the (001) and (110) planes. The periodic potential conditions were determined using conventional solid-state

pseudopotentials (PSLibrary_PAW_PBE). The cohesive energy was simulated using a $10 \times 10 \times 10$ Γ-centered k-mesh in a conventional hydroxyapatite crystal structure. Additionally, surface energies were simulated using a $5 \times 5 \times 1$ Γ-centered k-mesh in a five-layer stacked (001) surface with 20 of vacuum and a $4 \times 4 \times 1$ Γ-centered k-mesh in a three-layer stacked (110) surface with 20 of vacuum [(001) plane: 240 atoms, (110) plane: 298 atoms]. Moreover, crystal structure images were obtained using VESTA3 software.[51]

3. RESULTS AND DISCUSSION

HAp NPs were synthesized via a simple precipitation method by adjusting the titration rate of NaOH, as illustrated in Figure 1a. The morphology of HAp was easily controlled by adjusting the pH conditions during the synthesis process, which typically affects the electrostatic potential and surface energies of the facets in the HAp crystal. The initial pH of the mixed solution,

including calcium and phosphorus, was low (4.6). The pH gradually changed from 4.6 to 9.5 when NaOH was added in a dropwise manner for 24 h. In contrast, in the pouring process, the pH immediately increased to 7.5 and was maintained until the end of the reaction, as shown in Figure S1. These different synthetic pH environments induced different crystal growth in the p-HAP and r-HAp NPs, as shown in Figure 1b,c. The initial phase of r-HAp NPs involved tiny and spherical amorphous calcium phosphate (ACP) particles with sizes less than 50 nm, and this phase then transformed into the hexagonal apatite phase. (Figure 1d, Figures S2 and S3) In general, metastable ACP can easily transform to HAp through dissolution and recrystallization at high pH.[52] In contrast, the p-HAp NPs directly formed a hexagonal apatite phase owing to the introduction of appropriate pH conditions in which apatite is energetically stable,[53] followed by crystal growth with the initial plate morphology. To clarify the growth mechanism for p-HAp and r-HAp, the (001) and (110) facet surface energies of HAp and its $a(b)$-plane and c-plane molecular electrostatic potential were calculated using the Quantum Espresso module. The results are presented in Figure 1e and Table 1. Based on

Table 1. Comparison of Surface Energies of Different Facets of HAp

material	surface	surface energy (kg/s^2)
HAp	(001)	1.8950
	(110)	4.4864

the HAp crystal structure, the c-planes, perpendicular to the c-axis in the hexagonal channels, were negatively charged because the structure was rich in phosphate (PO_4^{3-}) and hydroxide ions (OH^-). In contrast, the $a(b)$-planes were abundant in positive calcium ions (Ca^{2+}), which affected the nucleation and growth of HAp through the electrostatic interaction with negatively charged OH^- ions. In the initial stage of dropwise addition, heterogeneous nucleation and growth were dominant as the OH^- ions restricted the growth of the (110) plane at low pH. The OH^- ions first adsorbed onto the (110) facet of HAp owing to its negative charge and

higher surface energy compared with those of other facets of HAp (Table 1), thereby limiting the Ca^{2+} and PO_4^{3-} interactions for growth in that facet.[54,55] Thus, the HAp nuclei preferred to grow parallel to the (110) direction, resulting in a plate morphology of the initial crystallite along the c-axis, as illustrated in Figure 1a. Subsequently, highly crystalline p-HAp was obtained after the reaction proceeded for 24 h. In contrast, the pouring of NaOH resulted in a high concentration of OH^- ions in the initial step, thereby influencing the homogeneous nucleation and growth of the primary particles. The abundance of OH^- ions led to growth along the c-axis owing to its stronger restrictive effect on the growth of positively charged facets ($a(b)$-planes), as depicted in Figure 1a, resulting in the formation of rod-shaped NPs during the phase transformation from ACP to HAp.[54−57] The crystallite size of both types of HAp was determined through XRD analysis, as shown in Figure S4. Typically, the (002) peak is employed for calculating the crystallite size of HAp due to its distinctive and sharp peak shape.[58−60] The p-HAp exhibited a smaller crystallite size of 26.8 nm, indicating lower crystallinity compared to that of the r-HAp (crystallite size: 38.7 nm). In addition, the crystallite sizes of both HAp types, calculated from (300) peaks, were smaller than those derived from the (002) peak, indicating growth along the c-axis.[58,59]

The structural characteristics of p-HAp and r-HAp were analyzed by HR-TEM. The p-HAP NPs exhibited a plate-type morphology with diameters ranging from 50 to 500 nm and thicknesses lower than 10 nm. In the SAED patterns (inset of Figure 2a), the bright pattern associated with the (002), (211), (112), and (300) planes indicated the presence of highly crystalline HAp. The d-spacings of p-HAp NPs were 0.344 and 0.278 nm with an angle of 36.2°, which were associated with the (002) and (112) crystal planes, respectively (Figure 2b), and indicated the $a(b)$-plane growth of HAp. Figure 2c shows the fast Fourier transform (FFT) patterns, which indicate that the (004), (002), (112), and (110) planes along the [1−10] zone axis demonstrate growth parallel to the c-axis. Figure 2d shows the rod-shaped particles with a d-spacing of 0.344 nm, corresponding to the (002) plane of HAp. (Figure 2e) The SAED pattern and FFT image can be indexed to the (211),
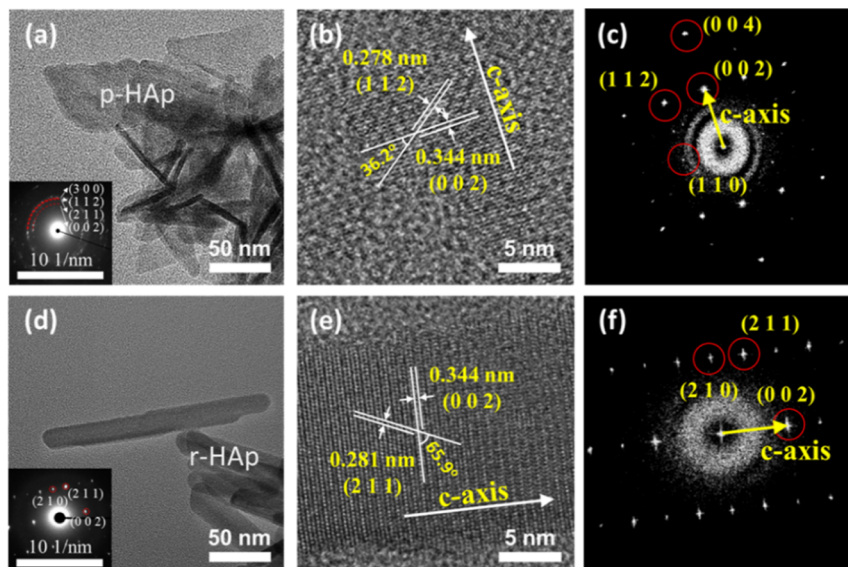

Figure 2. HR-TEM and FFT images of synthesized (a,c) p-HAp and (d−f) r-HAp. The insets of (a,d) show the corresponding SAED patterns.
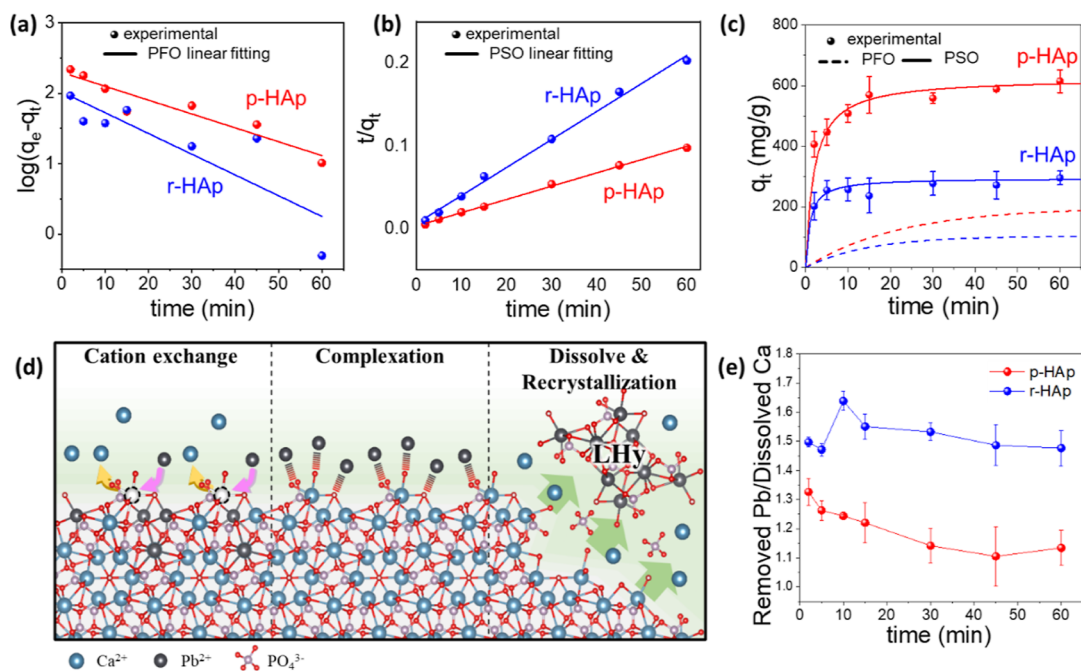
Figure 3. (a) Pb sorption kinetics of p-HAp and r-HAp fitted with PFO and PSO models, and linear fitting plots of the (b) PFO and (c) PSO models [Pb concentration: 2100 mg/m^3, HAp amounts: 1 mg/cm^3, reaction time: 60 min]. (d) Schematic of three mechanisms for Pb removal by HAp. (e) Ratio of the removed Pb to dissolved Ca during the removal process. A ratio larger than one indicates excess Pb removal compared to Ca dissolution, indicating the occurrence of surface complexation.
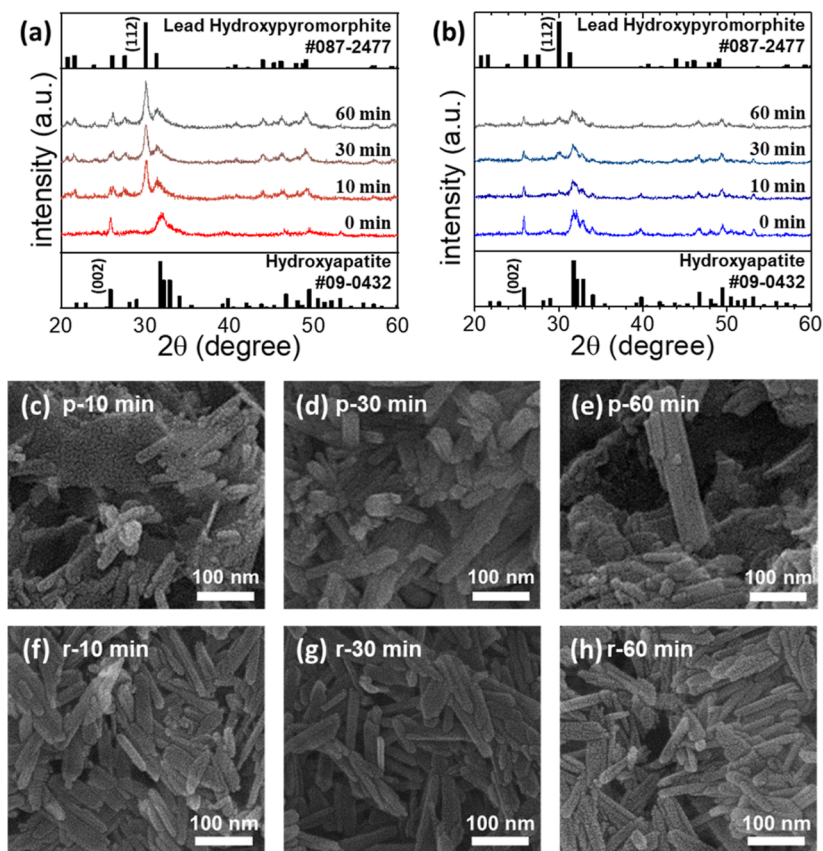

Figure 4. XRD patterns of (a) p-HAP and (b) r-HAp with different sorption time values. FE-SEM images of (c−e) p-HAP and (f−h) r-HAP after 10, 30, and 60 min of removal. (a,c−e) The shape and crystal structure of p-HAp change dramatically from HAp to LHy, whereas (b,f−h) those of r-HAp do not change significantly.
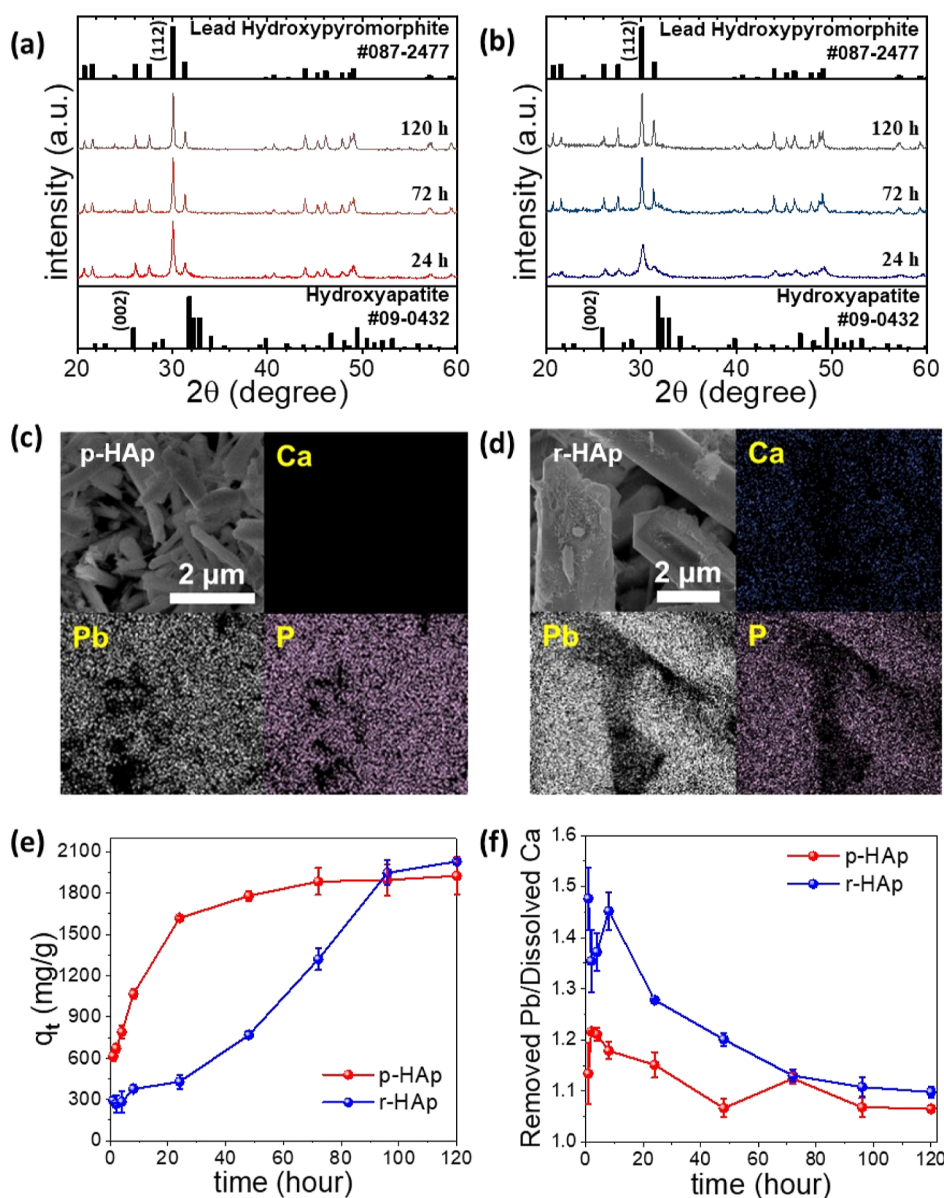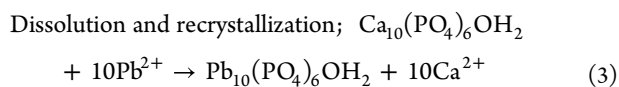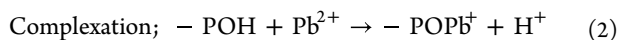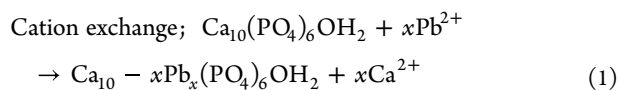
Figure 5. XRD patterns of (a) p-HAp and (b) r-HAp with different sorption time values. FE-SEM images and corresponding EDS mapping of (c) p-HAp and (d) r-HAp after sorption for 120 h. (e) Pb sorption kinetics of p-HAp and r-HAp [Pb concentration: 2100 mg/m³, HAp amount: 1 mg/cm³, reaction time: 120 h] and (f) ratio of removed Pb to dissolved Ca during the sorption process.

(210), and (002) planes of the crystalline hexagonal HAp structure, suggesting the occurrence of preferentially oriented growth along the [001] direction, as shown in Figure 2d–f. These results are consistent with the growth mechanism illustrated in Figure 1a.

The Pb removal capacities of both synthesized HAp NPs were evaluated at pH 5 in an aqueous solution over a period of 1 h. The sorption kinetics of p-HAp and r-HAp were investigated by fitting PFO and PSO models, as shown in Figure 3a–c. Both p-HAp and r-HAp were well fitted to the PSO kinetic model with higher linear regression coefficient (R^2) values than those of the PFO model (Figure 3a,b and Table S1), which indicated that the Pb removal process was dominated by chemisorption.[61] p-HAp exhibited slower adsorption kinetics than r-HAp, as evidenced by its lower second-order adsorption rate constant (k_2) of 8.28×10^{-4} g/mg min. However, p-HAp had a significantly higher expected maximum adsorption capacity ($q_{e,cal}$) of 625 mg/g compared

to r-HAp, which was well-validated by the experimental data. This adsorption capacity of p-HAp demonstrates a relatively high level, even in comparison with previously reported HAp (Table S3). The lower crystallinity observed in p-HAp (Figure S4) can contribute to an enhanced dissolution behavior, consequently resulting in a higher adsorption capacity.[32,33,62] This lower crystallinity also includes a large number of defects, facilitating ion exchange reactions between cations in HAp and the solution.[34] In addition, p-HAp had a slightly higher BET surface area of 111.88 ± 0.58 m²/g compared with that of r-HAp (101.01 ± 0.43 m²/g), along with a higher surface energy (Table 1). The surface potential of the $a(b)$-plane exhibited a charge that was more negative than that of the c-plane of HAp. In other words, the enhanced electrostatic interaction with positively charged Pb ions under these pH conditions resulted in the fast kinetics and large adsorption capacity of p-HAp (Table S2). To clarify the Pb removal reaction mechanism, we analyzed the characteristics of the Pb and Ca ions dissolved in

the aqueous solution during the Pb removal process. Figure 3d shows the three mechanisms of Pb removal by HAp, i.e., cation exchange, complexation, and dissolution/recrystallization, expressed as in eqs 1−3.

Cation exchange; $Ca_{10}(PO_4)_6OH_2 + xPb^{2+}$

$$\rightarrow Ca_{10} - xPb_x(PO_4)_6OH_2 + xCa^{2+} \qquad (1)$$

Complexation; $-POH + Pb^{2+} \rightarrow -POPb^+ + H^+ \qquad (2)$

Dissolution and recrystallization; $Ca_{10}(PO_4)_6OH_2$

$$+ 10Pb^{2+} \rightarrow Pb_{10}(PO_4)_6OH_2 + 10Ca^{2+} \qquad (3)$$

Typically, cation exchange and dissolution/recrystallization occur when Pb and Ca are exchanged in a ratio of 1/1, whereas surface complexation removes Pb without any loss of cations in the HAp structure. Thus, a Pb/Ca ratio approaching 1 indicates that cation exchange and dissolution/recrystallization are the dominant mechanisms for Pb removal, whereas a value higher than 1 suggests that surface complexation contributes to Pb removal.[63−65] As shown in Figure 3e, the Pb/Ca ratios were ~1.5 and 1.22 for r-HAP and p-HAp, respectively. In other words, the dominant removal mechanism for r-HAp was surface complexation and that for p-HAp was ion exchange and dissolution/recrystallization. Thus, the Pb removal capacities of r-HAp and p-HAp were expected to be different.

Figure 4a shows the XRD patterns of p-HAp and r-HAp NPs during the Pb removal process. For p-HAp, new peaks were observed at 21.56°, 26.04°, 27.48°, and 30.04°, which corresponded to the (111), (102), (210), and (112) planes of lead hydroxypyromorphite (LHy). The intensities of the (002) and (211) planes of HAp significantly decreased even in the reaction that lasted for only 10 min. The p-HAp NPs immediately transformed to rod-shaped LHy with lengths of a few hundred nanometers after Pb removal, as shown in Figure 4c−e. This dramatic morphology change was attributable to the occurrence of dissolution/recrystallization rather than complexation during the Pb removal process.[29,65] In comparison, the r-HAp NPs underwent a slow reaction with Pb ions. Thus, the HAp phase and morphology did not change considerably even after the 60 min reaction, as depicted in Figure 4b,f−h). This phenomenon can be attributed to pseudomorphism: The direct replacement of Ca^{2+} with Pb^{2+} by ion exchange helped preserve the initial shape and size of r-HAp.[66,67]

Over the reaction period, p-HAp transformed to a highly crystalline LHy phase, which was rod shaped with a length of several micrometers (Figures 5a and S5(a−c)). The EDS mapping and relative composition under different reaction periods were evaluated (Figure 5c,d, Figure S6, and Table S4). In the EDS mapping results of p-HAp, no Ca was detected after a reaction time of 72 h, suggesting that the p-HAp was completely transformed to LHy. In addition, as shown in Figure 5e, the Pb removal capacity of p-HAp reached equilibrium at the reaction time of 24 h, which indicated that p-HAp completely removed Pb by dissolution/recrystallization within 24 h. In contrast, r-HAp maintained its small rod shape with the coexistence of the low-crystalline HAp and LHy phases at 24 h, but a large rod shape with the highly crystalline LHy phase was obtained after 72 h (Figures 5b and S5(d−f)). The Pb removal capacity of r-HAP gradually increased after 120 h. In the kinetic curves of r-HAp, an

inflection point was observed at approximately 24 h (Figure 5e), suggesting a change in the Pb removal mechanism. Figure 5f shows the Pb/Ca ratio during the long-term Pb removal process. The high Pb/Ca ratio of r-HAp gradually decreased over time and approached that of p-HAp (approximately 1.1). This observation indicated that the dominant Pb removal mechanism of r-HAp changed from ion exchange in the initial stage to dissolution/recrystallization in the final stage. However, r-HAp exhibited the presence of Ca even after 120 h (Figure 5d), indicating an incomplete phase change to LHy. Consequently, p-HAp could remove Pb faster and better than r-HAp. Moreover, the final product after the removal reaction was pure LHy without any residual cations, which can promote Pb reuse or recycling.[29]

4. CONCLUSIONS

HAp with different morphologies (plate- and rod-shaped) was obtained, and the XRD pattern and TEM analysis results were consistent with the HAp crystal structure. We investigated the three removal mechanisms of the as-synthesized HAp: cation exchange, complexation, dissolution, and recrystallization. The Pb removal mechanisms of p-HAp and r-HAp were considerably different. For p-HAp, dissolution and recrystallization were predominantly observed from 10 min. In contrast, the dominant Pb removal mechanism of r-HAp changed from ion exchange to dissolution and recrystallization over time. Overall, the final dominant mechanism for both p-HAp and r-HAp was dissolution and recrystallization. Clarification of the Pb^{2+} removal mechanism is expected to facilitate the development of effective soil, air, and water purification strategies.

■ ASSOCIATED CONTENT

Ⓢ Supporting Information

The Supporting Information is available free of charge at https://pubs.acs.org/doi/10.1021/acsomega.3c07725.

Additional pH analysis, FE-SEM images, XRD, EDS mapping, adsorption kinetics analysis, BET, zeta potential, and table for adsorbent comparison (PDF)

■ AUTHOR INFORMATION

Corresponding Authors

Gill Sang Han − *Division of Advanced Materials, Korea Research Institute of Chemical Technology (KRICT), Daejeon 34114, Republic of Korea;* ⓞ orcid.org/0000-0002-3974-2138; Email: gshan@krict.re.kr

Hyun Suk Jung − *School of Advanced Materials Science & Engineering, Sungkyunkwan University, Suwon-si, Gyeonggi-do 16419, Republic of Korea; SKKU Institute of Energy Science and Technology (SIEST), Sungkyunkwan University, Suwon 16419, Republic of Korea;* ⓞ orcid.org/0000-0002-7803-6930; Email: hsjung1@skku.edu

Authors

Hee Jung Kim − *School of Advanced Materials Science & Engineering, Sungkyunkwan University, Suwon-si, Gyeonggi-do 16419, Republic of Korea*

Jin Hyuk Choi − *School of Advanced Materials Science & Engineering, Sungkyunkwan University, Suwon-si, Gyeonggi-do 16419, Republic of Korea*

SangMyeong Lee − *School of Advanced Materials Science & Engineering, Sungkyunkwan University, Suwon-si, Gyeonggi-do 16419, Republic of Korea*

Complete contact information is available at:
https://pubs.acs.org/10.1021/acsomega.3c07725

Author Contributions

ǁH.J.K. and J.H.C. contributed equally to this work.

Notes

The authors declare no competing financial interest.

■ ACKNOWLEDGMENTS

■ ABBREVIATIONS

ACP, amorphous calcium phosphate; EDS, energy dispersive spectroscopy; FFT, fast Fourier transform; PFO, pseudo-first-order; PSO, pseudo-second-order; SAED, selected area electron diffraction; TEM, transmission electron microscopy; XRD, X-ray diffraction

■ REFERENCES

(1) Xu, X.; Nie, S.; Ding, H.; Hou, F. F. Environmental pollution and kidney diseases. *Nat. Rev. Nephrol.* **2018**, *14* (5), 313−324.

(2) Kim, H.-S.; An, Y.-J.; Kwak, J. I.; Kim, H. J.; Jung, H. S.; Park, N.-G. Sustainable green process for environmentally viable perovskite solar cells. *ACS Energy Lett.* **2022**, *7* (3), 1154−1177.

(3) Zeng, X.; Xu, X.; Qin, Q.; Ye, K.; Wu, W.; Huo, X. Heavy metal exposure has adverse effects on the growth and development of preschool children. *Environ. Geochem. Health* **2019**, *41*, 309−321.

(4) Riaz, M. A.; Nisa, Z. U.; Anjum, M. S.; Butt, H.; Mehmood, A.; Riaz, A.; Akhtar, A. B. T. Assessment of metals induced histopathological and gene expression changes in different organs of non-diabetic and diabetic rats. *Sci. Rep.* **2020**, *10* (1), 5897.

(5) Rai, P. K.; Lee, S. S.; Zhang, M.; Tsang, Y. F.; Kim, K. H. Heavy metals in food crops: Health risks, fate, mechanisms, and management. *Environ. Int.* **2019**, *125*, 365−385.

(6) Park, H.; May, A.; Portilla, L.; Dietrich, H.; Münch, F.; Rejek, T.; Sarcletti, M.; Banspach, L.; Zahn, D.; Halik, M. Magnetite nanoparticles as efficient materials for removal of glyphosate from water. *Nat Sustainability* **2019**, *3* (2), 129−135.

(7) Kim, H. J.; Lee, J. M.; Choi, J. H.; Kim, D. H.; Han, G. S.; Jung, H. S. Synthesis and adsorption properties of gelatin-conjugated hematite (α-Fe2O3) nanoparticles for lead removal from wastewater. *J. Hazard. Mater.* **2021**, *416*, 125696.

(8) Grágeda, M.; González, A.; Grágeda, M.; Ushak, S. Purification of brines by chemical precipitation and ion-exchange processes for obtaining battery-grade lithium compounds. *Int. J. Energy Res.* **2018**, *42* (7), 2386−2399.

(9) Xu, Z.; Gu, S.; Rana, D.; Matsuura, T.; Lan, C. Q. Chemical precipitation enabled UF and MF filtration for lead removal. *J. Water Process Eng.* **2021**, *41*, 101987.

(10) Cai, Q. Q.; Wu, M. Y.; Li, R.; Deng, S. H.; Lee, B. C. Y.; Ong, S. L.; Hu, J. Y. Potential of combined advanced oxidation-Biological process for cost-effective organic matters removal in reverse osmosis concentrate produced from industrial wastewater reclamation: Screening of AOP pre-treatment technologies. *Chem. Eng. J.* **2020**, *389*, 123419.

(11) Licona, K. P. M.; Geaquinto, L. R. d. O.; Nicolini, J. V.; Figueiredo, N. G.; Chiapetta, S. C.; Habert, A. C.; Yokoyama, L. Assessing potential of nanofiltration and reverse osmosis for removal of toxic pharmaceuticals from water. *J. Water Process Eng.* **2018**, *25*, 195−204.

(12) Wu, J.; Wang, T.; Wang, J.; Zhang, Y.; Pan, W.-P. A novel modified method for the efficient removal of Pb and Cd from wastewater by biochar: Enhanced the ion exchange and precipitation capacity. *Sci. Total Environ.* **2021**, *754*, 142150.

(13) Tang, J.-H.; Jin, J.-C.; Li, W.-A.; Zeng, X.; Ma, W.; Li, J.-L.; Lv, T.-T.; Peng, Y.-C.; Feng, M.-L.; Huang, X.-Y. Highly selective cesium (I) capture under acidic conditions by a layered sulfide. *Nat. Commun.* **2022**, *13* (1), 658.

(14) Zeng, Q.; Hu, L.; Zhong, H.; He, Z.; Sun, W.; Xiong, D. Efficient removal of Hg2+ from aqueous solution by a novel composite of nano humboldtine decorated almandine (NHDA): Ion exchange, reducing-oxidation and adsorption. *J. Hazard. Mater.* **2021**, *404*, 124035.

(15) Sapkota, B.; Liang, W.; VahidMohammadi, A.; Karnik, R.; Noy, A.; Wanunu, M. High permeability sub-nanometre sieve composite MoS2 membranes. *Nat. Commun.* **2020**, *11* (1), 2747.

(16) Xie, X.; Chen, C.; Zhang, N.; Tang, Z.-R.; Jiang, J.; Xu, Y.-J. Microstructure and surface control of MXene films for water purification. *Nat Sustainability* **2019**, *2* (9), 856−862.

(17) Ling, S.; Qin, Z.; Huang, W.; Cao, S.; Kaplan, D. L.; Buehler, M. J. Design and function of biomimetic multilayer water purification membranes. *Sci. Adv.* **2017**, *3* (4), No. e1601939.

(18) Ritt, C. L.; Werber, J. R.; Deshmukh, A.; Elimelech, M. Monte Carlo simulations of framework defects in layered two-dimensional nanomaterial desalination membranes: implications for permeability and selectivity. *Environ. Sci. Technol.* **2019**, *53* (11), 6214−6224.

(19) Chen, W.; Lu, Z.; Xiao, B.; Gu, P.; Yao, W.; Xing, J.; Asiri, A. M.; Alamry, K. A.; Wang, X.; Wang, S. Enhanced removal of lead ions from aqueous solution by iron oxide nanomaterials with cobalt and nickel doping. *J. Cleaner Prod.* **2019**, *211*, 1250−1258.

(20) Oyewo, O. A.; Elemike, E. E.; Onwudiwe, D. C.; Onyango, M. S. Metal oxide-cellulose nanocomposites for the removal of toxic metals and dyes from wastewater. *Int. J. Biol. Macromol.* **2020**, *164*, 2477−2496.

(21) Ahmad, R.; Mirza, A. Facile one pot green synthesis of Chitosan-Iron oxide (CS-Fe2O3) nanocomposite: Removal of Pb(II) and Cd(II) from synthetic and industrial wastewater. *J. Cleaner Prod.* **2018**, *186*, 342−352.

(22) Gupta, S.; Sireesha, S.; Sreedhar, I.; Patel, C. M.; Anitha, K. L. Latest trends in heavy metal removal from wastewater by biochar based sorbents. *J. Water Process Eng.* **2020**, *38*, 101561.

(23) Gao, R.; Fu, Q.; Hu, H.; Wang, Q.; Liu, Y.; Zhu, J. Highly-effective removal of Pb by co-pyrolysis biochar derived from rape straw and orthophosphate. *J. Hazard. Mater.* **2019**, *371*, 191−197.

(24) Jin, Q.; Wang, Z.; Feng, Y.; Kim, Y. T.; Stewart, A. C.; O'Keefe, S. F.; Neilson, A. P.; He, Z.; Huang, H. Grape pomace and its secondary waste management: Biochar production for a broad range of lead (Pb) removal from water. *Environ. Res.* **2020**, *186*, 109442.

(25) Vesali-Naseh, M.; Vesali Naseh, M. R.; Ameri, P. Adsorption of Pb (II) ions from aqueous solutions using carbon nanotubes: A systematic review. *J. Cleaner Prod.* **2021**, *291*, 125917.

(26) Yang, K.; Lou, Z.; Fu, R.; Zhou, J.; Xu, J.; Baig, S. A.; Xu, X. Multiwalled carbon nanotubes incorporated with or without amino groups for aqueous Pb(II) removal: Comparison and mechanism study. *J. Mol. Liq.* **2018**, *260*, 149−158.

(27) Joseph, I. V.; Tosheva, L.; Doyle, A. M. Simultaneous removal of Cd(II), Co(II), Cu(II), Pb(II), and Zn(II) ions from aqueous

solutions via adsorption on FAU-type zeolites prepared from coal fly ash. *J. Environ. Chem. Eng.* **2020**, *8* (4), 103895.

(28) Xing, P.; Wang, C.; Ma, B.; Chen, Y. Removal of Pb(II) from aqueous solution using a new zeolite-type absorbent: Potassium ore leaching residue. *J. Environ. Chem. Eng.* **2018**, *6* (6), 7138–7143.

(29) Hong, J. S.; Kim, H. J.; Sohn, C. H.; Gong, O. Y.; Choi, J. H.; Cho, K. H.; Han, G. S.; Nam, K. T.; Jung, H. S. High-Throughput Pb Recycling for Perovskite Solar Cells Using Biomimetic Whitlockite. *Energy Environ. Mater.* **2022**, *6*, No. e12374.

(30) Park, S. Y.; Park, J.-S.; Kim, B. J.; Lee, H.; Walsh, A.; Zhu, K.; Kim, D. H.; Jung, H. S. Sustainable lead management in halide perovskite solar cells. *Nat Sustainability* **2020**, *3* (12), 1044–1051.

(31) Nayak, A.; Bhushan, B. Hydroxyapatite as an advanced adsorbent for removal of heavy metal ions from water: Focus on its applications and limitations. *Mater. Today: Proc.* **2021**, *46*, 11029–11034.

(32) Valizadeh, S.; Rasoulifard, M. H.; Dorraji, M. S. S. Adsorption and photocatalytic degradation of organic dyes onto crystalline and amorphous hydroxyapatite: Optimization, kinetic and isotherm studies. *Korean J. Chem. Eng.* **2016**, *33*, 481–489.

(33) Wei, W.; Zhang, X.; Cui, J.; Wei, Z. Interaction between low molecular weight organic acids and hydroxyapatite with different degrees of crystallinity. *Colloids Surf., A* **2011**, *392* (1), 67–75.

(34) Lei, Y.; Guan, J.-J.; Chen, W.; Ke, Q.-F.; Zhang, C.-Q.; Guo, Y.-P. Fabrication of hydroxyapatite/chitosan porous materials for Pb (II) removal from aqueous solution. *RSC Adv.* **2015**, *5* (32), 25462–25470.

(35) Xu, Y.; Tang, H.; Wu, P.; Chen, M.; Shang, Z.; Wu, J.; Zhu, N. Manganese-doped hydroxyapatite as an effective adsorbent for the removal of Pb (II) and Cd (II). *Chemosphere* **2023**, *321*, 138123.

(36) Bharath, G.; Jagadeesh Kumar, A.; Karthick, K.; Mangalaraj, D.; Viswanathan, C.; Ponpandian, N. Shape evolution and size controlled synthesis of mesoporous hydroxyapatite nanostructures and their morphology dependent Pb(ii) removal from waste water. *RSC Adv.* **2014**, *4* (70), 37446–37457.

(37) Srinivasan, M.; Ferraris, C.; White, T. Cadmium and lead ion capture with three dimensionally ordered macroporous hydroxyapatite. *Environ. Sci. Technol.* **2006**, *40* (22), 7054–7059.

(38) Zhou, M.; Yan, X.; Zou, H.; Zhao, Y.; Yin, N.; Zhang, C.; Wang, L. Enhanced adsorption of Pb(II) from aqueous solution by magnesium-incorporated hydroxyapatite with poor crystalline structure. *Desalin. Water Treat.* **2019**, *171*, 183–195.

(39) Garley, A.; Hoff, S. E.; Saikia, N.; Jamadagni, S.; Baig, A.; Heinz, H. Adsorption and Substitution of Metal Ions on Hydroxyapatite as a Function of Crystal Facet and Electrolyte pH. *J. Phys. Chem. C* **2019**, *123* (27), 16982–16993.

(40) Hao, L.; Lv, Y.; Song, H. The morphological evolution of hydroxyapatite on high-efficiency Pb2+ removal and antibacterial activity. *Microchem. J.* **2017**, *135*, 16–25.

(41) Hajimirzaee, S.; Chansai, S.; Hardacre, C.; Banks, C. E.; Doyle, A. M. Effects of surfactant on morphology, chemical properties and catalytic activity of hydroxyapatite. *J. Solid State Chem.* **2019**, *276*, 345–351.

(42) Jiang, J.; Long, Y.; Hu, X.; Hu, J.; Zhu, M.; Zhou, S. A facile microwave-assisted synthesis of mesoporous hydroxyapatite as an efficient adsorbent for Pb2+ adsorption. *J. Solid State Chem.* **2020**, *289*, 121491.

(43) Jenkins, R.; Snyder, R. L. *Introduction to X-ray Powder Diffractometry*; Wiley Online Library, 1996; Vol. *138*.

(44) Monshi, A.; Foroughi, M. R.; Monshi, M. R. Modified Scherrer equation to estimate more accurately nano-crystallite size using XRD. *World J. Nano Sci. Eng.* **2012**, *02* (03), 154–160.

(45) Deshiikan, S. R.; Papadopoulos, K. D. Modified Booth equation for the calculation of zeta potential. *Colloid Polym. Sci.* **1998**, *276*, 117–124.

(46) Simonin, J.-P. On the comparison of pseudo-first order and pseudo-second order rate laws in the modeling of adsorption kinetics. *Chem. Eng. J.* **2016**, *300*, 254–263.

(47) Feng, Y.; Gong, J.-L.; Zeng, G.-M.; Niu, Q.-Y.; Zhang, H.-Y.; Niu, C.-G.; Deng, J.-H.; Yan, M. Adsorption of Cd (II) and Zn (II) from aqueous solutions using magnetic hydroxyapatite nanoparticles as adsorbents. *Chem. Eng. J.* **2010**, *162* (2), 487–494.

(48) Wang, Y.-J.; Chen, J.-H.; Cui, Y.-X.; Wang, S.-Q.; Zhou, D.-M. Effects of low-molecular-weight organic acids on Cu (II) adsorption onto hydroxyapatite nanoparticles. *J. Hazard. Mater.* **2009**, *162* (2–3), 1135–1140.

(49) Jain, A.; Ong, S. P.; Hautier, G.; Chen, W.; Richards, W. D.; Dacek, S.; Cholia, S.; Gunter, D.; Skinner, D.; Ceder, G.; et al. Commentary: The Materials Project: A materials genome approach to accelerating materials innovation. *APL Mater.* **2013**, *1* (1), 011002.

(50) Hanwell, M. D.; Curtis, D. E.; Lonie, D. C.; Vandermeersch, T.; Zurek, E.; Hutchison, G. R. Avogadro: an advanced semantic chemical editor, visualization, and analysis platform. *J. Cheminf.* **2012**, *4* (1), 17.

(51) Momma, K.; Izumi, F. VESTA 3for three-dimensional visualization of crystal, volumetric and morphology data. *J. Appl. Crystallogr.* **2011**, *44* (6), 1272–1276.

(52) Han, G. S.; Lee, S.; Kim, D. W.; Kim, D. H.; Noh, J. H.; Park, J. H.; Roy, S.; Ahn, T. K.; Jung, H. S. A simple method to control morphology of hydroxyapatite nano-and microcrystals by altering phase transition route. *Cryst. Growth Des.* **2013**, *13* (8), 3414–3418.

(53) Koutsoukos, P.; Amjad, Z.; Tomson, M. B.; Nancollas, G. H. Crystallization of calcium phosphates. A constant composition study. *J. Am. Chem. Soc.* **1980**, *102* (5), 1553–1557.

(54) In, Y.; Amornkitbamrung, U.; Hong, M. H.; Shin, H. On the Crystallization of Hydroxyapatite under Hydrothermal Conditions: Role of Sebacic Acid as an Additive. *ACS Omega* **2020**, *5* (42), 27204–27210.

(55) Li, H.; Mei, L.; Liu, H.; Liu, Y.; Liao, L.; Kumar, R. V. Growth Mechanism of Surfactant-Free Size-Controlled Luminescent Hydroxyapatite Nanocrystallites. *Cryst. Growth Des.* **2017**, *17* (5), 2809–2815.

(56) Zhuang, Z.; Yamamoto, H.; Aizawa, M. Synthesis of plate-shaped hydroxyapatite via an enzyme reaction of urea with urease and its characterization. *Powder Technol.* **2012**, *222*, 193–200.

(57) Liu, J.; Li, K.; Wang, H.; Zhu, M.; Xu, H.; Yan, H. Self-assembly of hydroxyapatite nanostructures by microwave irradiation. *Nanotechnology* **2005**, *16* (1), 82–87.

(58) Zhang, H.-b.; Zhou, K.-c.; Li, Z.-y.; Huang, S.-p. Plate-like hydroxyapatite nanoparticles synthesized by the hydrothermal method. *J. Phys. Chem. Solids* **2009**, *70* (1), 243–248.

(59) Guo, X.; Xiao, P. Effects of solvents on properties of nanocrystalline hydroxyapatite produced from hydrothermal process. *J. Eur. Ceram. Soc.* **2006**, *26* (15), 3383–3391.

(60) Khalid, M.; Mujahid, M.; Amin, S.; Rawat, R. S.; Nusair, A.; Deen, G. R. Effect of surfactant and heat treatment on morphology, surface area and crystallinity in hydroxyapatite nanocrystals. *Ceram. Int.* **2013**, *39* (1), 39–50.

(61) Baby, R.; Saifullah, B.; Hussein, M. Z. Palm Kernel Shell as an effective adsorbent for the treatment of heavy metal contaminated water. *Sci. Rep.* **2019**, *9* (1), 18955.

(62) Wei, W.; Yang, L.; Zhong, W.; Cui, J.; Wei, Z. Poorly crystalline hydroxyapatite: A novel adsorbent for enhanced fulvic acid removal from aqueous solution. *Appl. Surf. Sci.* **2015**, *332*, 328–339.

(63) Mavropoulos, E.; Rossi, A. M.; Costa, A. M.; Perez, C. A. C.; Moreira, J. C.; Saldanha, M. Studies on the mechanisms of lead immobilization by hydroxyapatite. *Environ. Sci. Technol.* **2002**, *36* (7), 1625–1629.

(64) Guan, D.-X.; Ren, C.; Wang, J.; Zhu, Y.; Zhu, Z.; Li, W. Characterization of Lead Uptake by Nano-Sized Hydroxyapatite: A Molecular Scale Perspective. *ACS Earth Space Chem.* **2018**, *2* (6), 599–607.

(65) Zhou, C.; Wang, X.; Song, X.; Wang, Y.; Fang, D.; Ge, S.; Zhang, R. Insights into dynamic adsorption of lead by nano-hydroxyapatite prepared with two-stage ultrasound. *Chemosphere* **2020**, *253*, 126661.

(66) Kamiishi, E.; Utsunomiya, S. Nano-scale reaction processes at the interface between apatite and aqueous lead. *Chem. Geol.* **2013**, *340*, 121−130.

(67) Manecki, M.; Kwaśniak-Kominek, M.; Majka, J. M.; Rakovan, J. Model of interface-coupled dissolution-precipitation mechanism of pseudomorphic replacement reaction in aqueous solutions based on the system of cerussite $PbCO_3$ - pyromorphite $Pb_5(PO_4)_3Cl$. *Geochim. Cosmochim. Acta* **2020**, *289*, 1−13.